

# Dissipation in Films of Adsorbed Nanospheres Studied by Quartz Crystal Microbalance (QCM)

Diethelm Johannsmann,<sup>\*†</sup> Ilya Reviakine,<sup>‡,§</sup> and Ralf P. Richter<sup>‡,⊥</sup>

Institute of Physical Chemistry, Clausthal University of Technology, D-38678 Clausthal–Zellerfeld, Germany, Biosurfaces Unit, CIC biomaGUNE, 20009 Donostia, San Sebastian, Spain, Department of Biochemistry and Molecular Biology, University of the Basque Country, 48940 Leioa, Spain, and Department of New Materials and Biosystems, Max Planck Institute for Metals Research, D-70569 Stuttgart, Germany

The quartz crystal microbalance (QCM) has become a popular method to study the formation of surface-confined films that consist of discrete biomolecular objects—such as proteins, phospholipid vesicles, virus particles—in liquids. The quantitative interpretation of QCM data—frequency and bandwidth (or, equivalently, dissipation) shifts—obtained with such films is limited by the lack of understanding of the energy dissipation mechanisms that operate in these films as they are sheared at megahertz frequencies during the QCM experiment. Here, we investigate dissipation mechanisms in such films experimentally and by finite-element method (FEM) calculations. Experimentally, we study the adsorption of globular proteins and virus particles to surfaces with various attachment geometries: direct adsorption to the surface, attachment via multiple anchors, or attachment via a single anchor. We find that the extent of dissipation caused by the film and the evolution of dissipation as a function of surface coverage is not dependent on the internal properties of these particles but rather on the geometry of their attachment to the surface. FEM calculations reproduce the experimentally observed behavior of the dissipation. In particular, a transient maximum in dissipation that is observed experimentally is reproduced by the FEM calculations, provided that the contact zone between the sphere and the surface is narrow and sufficiently soft. Both a small-angle rotation of the sphere in the flow field of the background fluid (rocking) and a small-amplitude slippage (sliding) contribute to the dissipation. At high coverage, lateral hydrodynamic interactions between neighboring spheres counteract these modes of dissipation, which results in a maximum in dissipation at intermediate adsorption times. These results highlight that, in many scenarios of biomolecular adsorption, the dissipation is not primarily determined by the adsorbate itself, but rather by the link by which it is bound to the substrate.

Adsorption to planar surfaces is a process of prime importance in various areas of analytics. Bioanalytics and rapid screening technologies, in particular, heavily rely on the affinity of a target substance to a suitably functionalized surface.<sup>1</sup> In most instances, the amount of adsorbed material is the central parameter of interest. This parameter is dependent on time, analyte concentration, the type of surface functionalization, and environmental parameters such as temperature or pH. In the case of soft analytes (proteins, viruses, vesicles), the intrinsic properties of these adsorbed objects, as well as the modalities of surface attachment, are also of interest.

Determining all the details of an adsorbate's amount, shape, orientation, and internal structure is certainly a challenge. One cannot hope to obtain such a detailed picture with any single sensing technique. Combining approaches based on different sensing principles<sup>2–7</sup> offers a more realistic representation of the adsorbate's organization on the surface. By virtue of their principles of operation, acoustic techniques (quartz crystal microbalances, abbreviated as QCMs,<sup>8–10</sup> shear-horizontal surface acoustic wave devices, abbreviated as SH-SAW devices,<sup>11,12</sup> and Love-wave devices<sup>13</sup>) are sensitive to intrinsic mechanical properties of the adsorbed layers and can provide information that is not easily accessible by other techniques.

The experiments reported below were undertaken with a QCM, but the argument applies to other acoustic sensors in essentially the same way. When a shear wave hits the interface between the resonator and the sample, it experiences a phase

\* Author to whom correspondence should be addressed. E-mail: johannsmann@pc.tu-clausthal.de.

<sup>†</sup> Institute of Physical Chemistry, Clausthal University of Technology.

<sup>‡</sup> Biosurfaces Unit, CIC biomaGUNE.

<sup>§</sup> Department of Biochemistry and Molecular Biology, University of the Basque Country.

<sup>⊥</sup> Department of New Materials and Biosystems, Max Planck Institute for Metals Research.

- (1) Cooper, M. A. *Anal. Bioanal. Chem.* **2003**, *377*, 834.
- (2) Domack, A.; Prucker, O.; et al. *Phys. Rev. E* **1997**, *56*, 680.
- (3) Reimhult, E.; Larsson, C.; Kasemo, B.; Höök, F. *Anal. Chem.* **2004**, *76*, 7211.
- (4) Bingen, P.; Wang, G.; Steinmetz, N. F.; Rodahl, M.; Richter, R. P. *Anal. Chem.* **2008**, *80*, 8880.
- (5) Rojas, E.; Gallego, M.; Reviakine, I. *Anal. Chem.* **2008**, *80*, 8982.
- (6) Laschitsch, A.; Menges, B.; Johannsmann, D. *Appl. Phys. Lett.* **2000**, *77*, 2252.
- (7) Edvardsson, M.; Svedhem, S.; Wang, G.; Richter, R.; Rodahl, M.; Kasemo, B. *Anal. Chem.* **2009**, *81*, 349.
- (8) Cady, W. G. *Piezoelectricity*; McGraw–Hill: New York, 1946.
- (9) Johannsmann, D. In *Piezoelectric Sensors*; Steinem, C., Janshoff, A., Eds.; Springer: New York, 2006; p 49.
- (10) Rodahl, M.; Hook, F.; Krozer, A.; et al. *Rev. Sci. Instrum.* **1995**, *66*, 3924.
- (11) Martin, F.; Newton, M. I.; McHale, G.; Melzak, Ka. A.; Gizeli, E. *Biosens. Bioelectr.* **2004**, *19*, 627.
- (12) Gulyaev, Y. V. *IEEE Trans. Ultrason. Ferroelectr. Freq. Control* **1998**, *45*, 935.
- (13) McMullan, C.; Gizeli, E.; Mehta, H.; Lowe, C. R. *J. Phys. D: Appl. Phys.* **2000**, *33*, 3053.

shift as well as an attenuation. The phase shift is proportional to the film thickness (or, in the case of a heterogeneous adsorbate, some equivalent parameter proportional to the adsorbed amount), while the attenuation is proportional to the energy dissipated inside the sample. For the QCM, the phase shift leads to a shift in the resonance frequency ( $\Delta f$ ), whereas the attenuation increases the bandwidth of the resonance ( $2\Delta\Gamma$ ). Some advanced QCMs output motional resistance,  $R_1$ , or the dissipation,  $D$ , instead of the bandwidth. These parameters are essentially equivalent.<sup>14,15</sup> They are related by<sup>16</sup>

$$D = \left(\frac{2}{f}\right)\Gamma \quad (1a)$$

$$R_1 = \left(\frac{\pi}{16A_{\text{eff}}f_{\text{F}}^3Z_{\text{q}}d_{26}^2}\right)\Gamma \quad (1b)$$

Here,  $A_{\text{eff}}$  is the effective electrode area (close to the area of the back electrode),  $f_{\text{F}}$  the frequency of the fundamental,  $Z_{\text{q}}$  the acoustic impedance of AT-cut quartz ( $Z_{\text{q}} = 8.8 \times 10^6 \text{ kg/(m}^2 \text{ s)}$ ), and  $d_{26}$  the piezoelectric strain coefficient ( $d_{26} = 3.1 \text{ pm/V}$ ). These parameters are related to the dissipated energy via the relation

$$\Delta D = \Delta(Q^{-1}) = \frac{\dot{E}}{\omega E}$$

where  $Q$  is the quality factor,  $\dot{E}$  the rate of energy dissipation in the sample, and  $E$  the entire energy contained in the resonator's movement. This last relation makes it clear that the quantitative interpretation of QCM data, in terms of the amount of analyte and its properties, requires some knowledge of the mechanism by which the energy in the adsorbed layer is dissipated. The mechanism of energy dissipation in adsorbed layers consisting of spatially separated objects that exhibit aspect ratios close to unity is the focus of this work. Such configurations occur when globular proteins or other nanosized particles adsorb or are attached to surfaces. For simplicity, we call these layers heterogeneous, referring, in particular, to the spatial heterogeneity of discrete adsorbed objects.

For planar, laterally homogeneous films, the acoustic models underlying the interpretation of  $\Delta f$  and  $\Delta\Gamma$ , in terms of the viscoelastic properties of the layer, are well-established.<sup>17–22</sup> In this approach, the energy stored/lost in the layer is parametrized in terms of frequency-dependent elastic and viscous compliances  $J'$  and  $J''$ , which, in turn, are related to the storage and loss moduli  $G'$  and  $G''$ . Many experiments can be analyzed with somewhat

simplified models, applicable to the thin-film limit. Films are considered thin if their thickness is much less than the depth of penetration of the shear wave, which is 250 nm for a 5-MHz resonator in water. For a thin film in liquid, the ratio of  $\Delta\Gamma$  and  $-\Delta f$  (which we term the “Df ratio”) is independent of the film thickness. It is a materials parameter. More specifically, one has the relation<sup>23</sup>

$$\frac{\Delta\Gamma}{(-\Delta f)} \approx J'\omega\eta_{\text{liq}} \quad (2)$$

where  $J'$  is the elastic compliance of the film and  $\eta_{\text{liq}}$  is the viscosity of the liquid.<sup>24</sup>

For spatially heterogeneous films, the essential question is this: Where is the energy dissipated? One possibility is that the energy is dissipated inside the adsorbate particles in essentially the same way as in a bulk film. The dissipation would then be proportional to a particle's elastic compliance and surface coverage. One would then treat the sample as an “equivalent planar film” and apply the respective equations (such as eq 2). However, the equivalent parameters derived within such a model must be interpreted with care. Indeed, it is increasingly becoming clear that this continuum approach is inadequate for heterogeneous films.<sup>5,25,26</sup>

In what follows, we demonstrate experimentally that another energy dissipation mechanism dominates in heterogeneous films. This mechanism is related to the mechanical properties of the contact zone between the adsorbed particles and the resonator surface, rather than to the mechanical properties of the particles themselves. We then use finite-element method (FEM) calculations to investigate this energy dissipation mechanism in detail. The interaction with the surrounding liquid causes the adsorbed particles to move (rock and slide). The degree to which the particles move is dependent on the mechanical properties of the contact zone between the particle and the substrate. While one might think that most energy is dissipated inside the contact zone, the FEM calculation shows that this is not true. Most of the energy (>90%) is dissipated in the liquid, even though the contact zone controls the motion. Because the contact zone determines the dissipation, the dissipation (or bandwidth) provides information about the linkage between these particles and the surface, rather than the particles themselves.

## EXPERIMENTAL SECTION

It is instructive to recall some experimental observations, reported by us and others in several *a priori*, unrelated publications that are of direct interest in the context of this study. They pertain to the dissipation induced upon the adsorption of globular proteins in submonolayer quantities on smooth surfaces. Experiments reported in the following were performed with a QCM-D setup (Q-Sense AB). Therefore, for the convenience of the user,

- (14) Johannsmann, D. *Phys. Chem. Chem. Phys.* **2008**, *10*, 4516.  
 (15) The ratio of motional resistance ( $R_1$ ) and dissipation ( $D$ ) should be constant (based on the Butterworth–van Dyke equivalent circuit). It is experimentally observed, however, that the ratio can fluctuate slightly.  
 (16) Johannsmann, D.; Heim, L. O. *J. Appl. Phys.* **2006**, *100*, 094505.  
 (17) Johannsmann, D.; Mathauer, K.; Wegner, G.; Knoll, W. *Phys. Rev. B* **1992**, *46*, 7808.  
 (18) Johannsmann, D. *Macromol. Chem. Phys.* **1999**, *200*, 501 (eq 13).  
 (19) Nakamoto, T.; Moriizumi, T. *Jpn. J. Appl. Phys.* **1990**, *29*, 963.  
 (20) Bandy, H. L.; Martin, S. J.; Cernosek, R. W.; Hillman, A. R. *Anal. Chem.* **1999**, *71*, 2205.  
 (21) Lucklum, R.; Behling, C.; Hauptmann, P. *Anal. Chem.* **1999**, *71*, 2488.  
 (22) Voinova, M. V.; Rodahl, M.; Jonson, M.; Kasemo, B. *Phys. Scr.* **1999**, *59*, 391.

- (23) Du, B. Y.; Johannsmann, D. *Langmuir* **2004**, *20*, 2809.  
 (24) Historically, the Df ratio was first used in the context of nanotribology. For a layer of rigid spheres adsorbed to a solid surface from vacuum, the Df ratio is proportional to the momentum relaxation time or “slip time”. For details, see: (a) Krim, J.; Widom, A. *Phys. Rev. B* **1988**, *38*, 12184. (b) Krim, J. *Nano Today* **2007**, *2*, 38.  
 (25) Johannsmann, D.; Reviakine, I.; Rojas, E.; Gallego, M. *Anal. Chem.* **2008**, *80*, 8891.  
 (26) Tellechea, E.; Johannsmann, D.; Steinmetz, N. F.; Richter, R. P.; Reviakine, I. *Langmuir* **2009**, *25*, 5177.

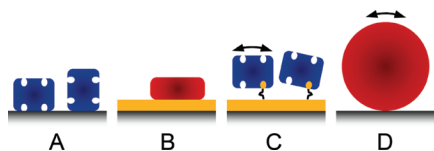


**Figure 1.** Schematic illustrations of different adsorption/binding geometries: (A and B) Adsorbates that attach to the underlying substrate via an extended contact area. (This case includes the direct adsorption of avidin, streptavidin, and ferritin to gold (panel A) and binding of annexin A5 to a supported lipid bilayer (SLB) (panel B) and corresponds to low dissipation, as discussed in the text.) (C) Adsorbates are attached to the surface via a flexible linker, corresponding to the case of streptavidin or avidin bound to a biotinylated SLB and His-tagged GFP to NTA-functionalized SLBs. (D) Adsorbates bind to the surface via a limited contact area. (This corresponds to the case of CPMV adsorbed on gold.) The particles depicted in panels C and D have more freedom to move (rock or slide), as compared to the scenarios depicted in panels A and B.

we use the dissipation  $D = Q^{-1}$  to quantify bandwidth ( $\Delta\Gamma/n = 2.5 \times 10^6 \text{ Hz} \times \Delta D$  for a 5 MHz sensor crystal).

The first case in point is the binding of the protein annexin A5 to solid-supported lipid bilayers (SLBs).<sup>27,28</sup> The dissipation shift observed in this case is around  $\Delta D = 0.2 \times 10^{-6}$ , which is close to the detection limit. Annexin A5 is not unique in producing very small dissipation shifts. We have recently found responses of  $\Delta D \approx 0.2 \times 10^{-6}$  for three other proteins on clean gold surfaces: avidin (Av),<sup>29</sup> streptavidin (SAv),<sup>29</sup> and purified ferritin.<sup>5</sup>

For a large number of protein adsorption scenarios, however, higher dissipation shifts, with a magnitude of typically  $\sim 1.0 \times 10^{-6}$ , have been reported. Notably, a response of  $0.8 \times 10^{-6}$  is typically observed upon binding of Av and SAv on biotin-functionalized SLBs.<sup>4,30</sup> The several-fold-higher dissipation for these two proteins on SLBs, as compared with the same proteins on gold, indicates that there must exist a pathway of energy dissipation that is connected not with the intrinsic properties of the proteins, but with the way they are coupled to the surface. This point is illustrated in Figure 1, where a schematic overview of typical binding geometries is shown. The dissipation is smallest when proteins are in firm contact with the underlying surface. For example, annexin A5 is known from structural analysis to associate very tightly with the SLBs (see Figure 1B),<sup>31,32</sup> and Av and SAv with their cuboid shape are also likely to physisorb to gold with one of their faces (see Figure 1A). The biotin-moiety on the SLB, on the other hand, contains a flexible spacer, about a nanometer in length, around which the proteins can potentially rotate (see Figure 1C).

We stress that, in both situations, the proteins are in near-native conformations. This is confirmed by direct structural analysis of membrane-bound annexin A5,<sup>31,32</sup> by the fact that immobilized Av and SAv retain their ability to bind biotin, and by the fact that ferritin is not significantly compressed upon adsorption.<sup>25</sup> Therefore, the intrinsic rigidity of these globular proteins

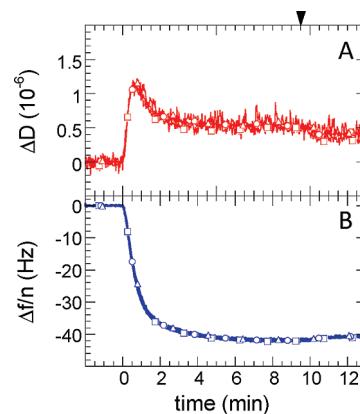


**Figure 2.** Adsorption curves, as measured by QCM-D, for the binding of His-tagged green fluorescence protein (His-GFP) to an NTA-functionalized SLB. Data for (A) the dissipation and (B) the normalized frequency ( $\Delta f/n$ , for  $\square$   $n = 5$ ,  $\circ$   $n = 9$ , and  $\triangle$   $n = 13$ ) are shown. A transient peak in the dissipation between 0 min and 1 min is clearly visible. SLBs were made from small unilamellar vesicles that contain dioleoylphosphatidylcholine (DOPC) and 10 mol % dioleoylglycerosuccinyl-nitrilotriacetic acid (DOGS-NTA). (See ref 65 for vesicle preparation and SLB-formation.) His-GFP incubation at 20  $\mu\text{g/mL}$  started at 0 min, after  $\text{Ni}^{2+}$  loading of the NTA-functionalized SLB in 5 mM  $\text{NiCl}_2$  (not shown). Washing in buffer is indicated by the arrowhead.

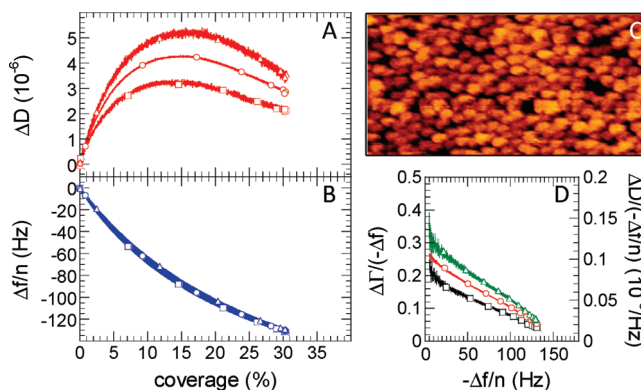


**Figure 3.** Responses in (A) dissipation and (B) frequency, as a function of surface coverage for the physisorption of CPMV onto a gold surface. Data for  $\square$   $n = 5$ ,  $\circ$   $n = 9$ , and  $\triangle$   $n = 13$  are shown. The coverage was determined by parallel reflectometry measurements. (C) Atomic force microscopy (AFM) image ( $1 \mu\text{m} \times 0.5 \mu\text{m}$ ) of the surface morphology after the measurement. The particles, visible as protrusions of a few 10 nm in diameter, cover the surface homogeneously but form an irregular array. No local clustering, e.g., into hexagonally packed islands, is observed. (D)  $\Delta\Gamma/(-\Delta f)$  ratios (also called Df ratios), as a function of frequency for the same adsorption process. Adapted from refs 4 and 26.

is in itself too high to induce appreciable dissipation of energy at MHz frequencies. To the QCM, these globular proteins appear as rigid particles.

Another peculiar feature that has been observed repeatedly in the dissipation response is the appearance of a transient peak. Such transient peaks are illustrated in Figures 2A and 3A for two different systems: His-tagged green fluorescent protein (GFP) binding to a nitrilotriacetic acid (NTA)-functionalized SLB (Figure 2), and cowpea mosaic virus (CPMV) adsorbing on a bare gold surface (Figure 3; see Figure 1D for the binding

(27) Richter, R. P.; Brisson, A. *Langmuir* **2004**, *20*, 4609.  
 (28) Richter, R. P.; Lai Kee Him, J.; Tessier, B.; Tessier, C.; Brisson, A. *Biophys. J.* **2005**, *89*, 3372.  
 (29) Wolny, P.; Spatz, J. P.; Richter, R. P. *Langmuir* **2009**, in press.  
 (30) Höök, F.; Ray, A.; Nordén, B.; Kasemo, B. *Langmuir* **2001**, *17*, 8305.  
 (31) Brisson, A.; Mosser, G.; Huber, R. *J. Mol. Biol.* **1991**, *220*, 199.  
 (32) Reviakine, I.; Bergsma-Schutter, W.; Mazeret-Dubut, C.; et al. *J. Struct. Biol.* **2000**, *131*, 234.

geometry).<sup>4,26,33</sup> In the case of Figure 3, coverage is available from the experiment, because the adsorption was monitored by an optical technique in parallel to the acoustic measurements.<sup>4</sup> For the experiment shown in Figure 2, no such parallel optical measurement was made. Here, frequency and dissipation are plotted versus time, rather than coverage. It is reasonable to assume that coverage increases monotonically with time. Essentially, the dissipation increases until some intermediate coverage, and then decreases as the coverage continues to increase. No corresponding minimum in the frequency shift is observed. Therefore, these transient peaks should not be confused with the appearance of the local extrema *in both frequency and dissipation shifts* that indicate transformations in the structure of the adsorbed films—such as, for example, the adsorbed vesicle-to-bilayer transition described by Keller et al.<sup>34</sup>

Initially, transient peaks in dissipation were observed by Höök et al. during binding of SA<sub>v</sub> to a biotinylated SLB,<sup>30</sup> and it was proposed that such behavior is characteristic of the transition between the disordered and the crystalline phases of streptavidin (the phase behavior of SA<sub>v</sub> on lipid bilayers is discussed in ref 35 and also is noted in ref 36). However, many other examples of transient peaks in dissipation can be found in the literature: they include adsorption of Av to biotinylated SLBs,<sup>4</sup> specific binding of prothrombin to negatively charged SLBs,<sup>37</sup> adsorption of vesicles to surfaces without their subsequent rupture,<sup>38</sup> and, now, the two examples shown in Figures 2 and 3. None of these systems exhibit any evidence of structural or conformational transitions of the type expected for the streptavidin system. Indeed, Av does not crystallize on biotinylated lipid layers;<sup>39</sup> similarly, we are not aware of any evidence suggesting that His-tagged GFP or prothrombin self-organize when bound to SLBs. CPMV is approximately a sphere with a diameter of ~28 nm, whose shape is most likely preserved upon adsorption, because of the virus' mechanical stability (see Figure 1D).<sup>40</sup> Direct imaging, using AFM (see Figure 3C), confirmed the formation of a monolayer of predominantly isolated virus particles; the particles did not move laterally and extended clusters could not be found.<sup>4</sup> Given that the peak occurs for such a diversity of systems, one may wonder if it can indeed be explained uniquely by specific intermolecular interactions.

To gain insight into the mechanism behind energy dissipation in heterogeneous systems, and the distinct dissipation peak, we sought to reproduce our experimental results using FEM calculations. We chose the adsorption of CPMV on gold (Figure 3) as the benchmark to compare the modeling results and stress the following observations that a model should reproduce:

(i) The dissipation increases as the overtone order increases, with values up to  $5 \times 10^{-6}$  (at  $n = 13$ ).

(ii) The maximum in dissipation occurs at a surface coverage of ~10%–20%<sup>4</sup> and becomes more pronounced with increasing overtone order.

(iii) The frequency shift shows no peak and only very little dependence on the overtone order.

(iv) The absolute ratio between dissipation (or bandwidth) shift and frequency shift decreases with increasing absolute frequency shift in a close-to-linear fashion (see Figure 3D). Extrapolation of the lines for different overtones leads to a common intercept at vanishing dissipation.<sup>26</sup>

We remark that this behavior seems to be characteristic of films comprised of discrete objects (nanoparticles) with an aspect ratio close to unity. It is strikingly different from that of homogeneous films or films of elongated, rodlike particles. For an interesting recent example of the latter, we refer the reader to the work of Tsortos et al. on films of grafted DNA, where the D<sub>f</sub> ratio is observed to be independent of surface coverage and related to the intrinsic viscosity of the DNA molecules.<sup>41,42</sup>

## MODELING

The calculation of the frequency shifts ( $\Delta f$ ) and shifts of the bandwidth ( $\Delta \Gamma$ ) was based on the small-load approximation (SLA):

$$\frac{\Delta f^*}{f_F} = \left( \frac{i}{\pi Z_q} \right) Z_L = \left( \frac{i}{\pi Z_q} \right) \frac{\langle \sigma \rangle}{\dot{u}} \quad (3)$$

Here,  $\Delta f^*$  is the complex frequency shift ( $\Delta f^* = \Delta f + i\Delta \Gamma$ ),  $f_F$  the frequency of the fundamental,  $Z_q$  the acoustic impedance of AT cut quartz ( $Z_q = 8.8 \times 10^6 \text{ kg}/(\text{m}^2 \text{ s})$ ),  $Z_L$  the load impedance,  $\langle \sigma \rangle$  the laterally averaged tangential stress, and  $\dot{u}$  the lateral speed at the crystal surface. The stress has an in-phase component and an out-of-phase component; therefore, eq 3 is complex.

SLA is applicable to a wide variety of samples. This certainly includes simple samples such as the Sauerbrey film or the Newtonian liquid.<sup>14</sup> Importantly, SLA can also be applied to laterally heterogeneous samples, because it builds on the *average* tangential stress,  $\langle \sigma \rangle$ . The stress may be calculated analytically for simple geometries such as the Sauerbrey film, but it may also be calculated by numerical means, in case such analytical equations do not exist, as we do in this case. Inserting the average stress into eq 3, one obtains the complex frequency shift.

The average tangential stress,  $\langle \sigma \rangle = \langle \eta \partial v_x / \partial z \rangle$  (where  $\eta$  is the viscosity and  $v$  is the speed), on the resonator surface was calculated from the velocity fields obtained numerically using FEM performed with the Multiphysics software package (COMSOL GmbH, Göttingen, Germany). The methodology has been described in detail in ref 25; however, we describe it here again, for the sake of clarity and because the procedure used in this work is slightly different.

In short, a cell is defined as shown in Figure 4A. It contains a planar layer, a particle, and an ambient liquid. The particle is a truncated sphere (more precisely, a truncated cylinder; see

(33) Steinmetz, N. F.; Bock, E.; Richter, R. P.; Spatz, J. P.; Lomonosoff, G. P.; Evans, D. J. *Biomacromolecules* **2008**, *9*, 456.

(34) Keller, C. A.; Kasemo, B. *Biophys. J.* **1998**, *75*, 1397.

(35) Frey, W.; Scheif, W.; Vogel, V. *Langmuir* **1996**, *12*, 1312.

(36) Direct evidence for 2D crystallization on SLB-coated QCM-D sensors is still missing. It may potentially be obstructed by the nanometer-scale roughness of the sensor surface, as demonstrated for other proteins; see ref 28.

(37) Richter, R. P.; Maury, N.; Brisson, A. *Langmuir* **2005**, *21*, 299.

(38) Reviakine, I.; Rossetti, F. F.; Morozov, A. N.; et al. *J. Chem. Phys.* **2005**, *122*, 204711.

(39) Horton, M. R.; Reich, C.; Gast, A. P. *Langmuir* **2007**, *23*, 6263.

(40) Roos, W. H.; Ivanovska, I. L.; Evilevitch, A.; Wuite, G. J. *Cell. Mol. Life Sci.* **2007**, *64*, 1484.

(41) Tsortos, A.; Papadakis, G.; Mitsakakis, K.; Melzak, K. A.; Gizeli, E. *Biophys. J.* **2008**, *94*, 2706–2715.

(42) Tsortos, A.; Papadakis, G.; Gizeli, E. *Biosens. Bioelectron.* **2008**, *24*, 842–847.

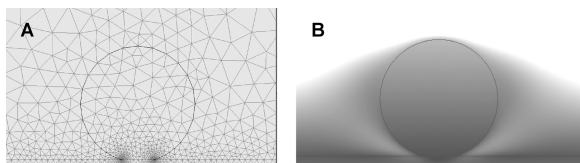


**Figure 4.** Two-dimensional view of the simulation cell geometry and a typical solution of the FEM calculations. The simulation cell contains a particle with a radius of 14 nm, and a spacer layer 2 nm thick. ((A) Mesh employed for the FEM calculation and (B) speed of lateral flow.) Dark colors correspond to a speed identical to the speed of the substrate. The gray scale was adjusted to visualize the variability of lateral speed close to the sphere. White areas are offscale.

description below) with a diameter ( $d$ ) of 28 nm. The length of the contact line is 7.4 nm. This geometry is intended to mimic an adsorbed CPMV nanoparticle; however, the qualitative outcome of the calculation applies to a wide variety of adsorbates. The resonator surface corresponds to the cell boundary at the bottom. The figure only covers the portion of the cell close to the particle. The cell extends to the top, far beyond the range displayed, having a height of  $2\ \mu\text{m}$ , which is 8 times the penetration depth of the acoustic shear wave at 5 MHz. Also, in many cases, the cell was much wider than the range displayed in Figure 4. The width varied over a range of 30–470 nm. The ambient liquid was Newtonian with a viscosity of 1 mPa s.

With the computational resources available to us, we could only compute the properties of a two-dimensional (2D) model; i.e., the circle in Figure 4 corresponds to a cylinder rather than a sphere. COMSOL can, in principle, also perform three-dimensional (3D) calculations. However, one cannot afford the required mesh size on a personal computer. Clearly, a 2D model cannot provide a truly realistic description of the flow profile. The flow around a sphere is certainly different from the flow around a cylinder. As in refs 25 and 26, we calculated the flows around cylinders lying parallel and perpendicular to the direction of flow, and then approximated the 3D situation by taking an arithmetic average of the frequency and bandwidth shift obtained in the two situations. In the particular case presented here, parallel and perpendicular flow actually yield similar results and, therefore, the averaging procedure is not essential.

The flow perpendicular to the cylinder axes (parallel to the plane of the paper in Figure 4) was calculated using the 2D steady-state incompressible Navier–Stokes module. The resonator surface performs an oscillatory motion. More precisely, it is assigned a fixed “speed” of  $i\omega u_0$ , where  $u_0$  is the amplitude of motion ( $u_0 = 10^{-2}$  nm). The frequency ( $\omega$ ) is  $2\pi n \times 5$  MHz, where  $n$  is the overtone order. A small amplitude of motion was chosen to avoid nonlinear effects. Although the flow profile is nontrivial, the flow is by no means turbulent. The flow is strictly laminar (in experiment and in the model). Apart from the nonlinear term in the Navier–Stokes equation, nonlinearities might also come about because the model uses a stationary mesh. Strictly speaking, a stationary mesh (with stationary domain boundaries) is inapplicable to a situation where the particle itself can move. As proven in the supporting information to ref 25, the error introduced by the fixed subdomain boundaries vanishes in the small-amplitude limit. The error is quadratic in amplitude, whereas all other quantities scale linearly with amplitude. Periodic boundary conditions are

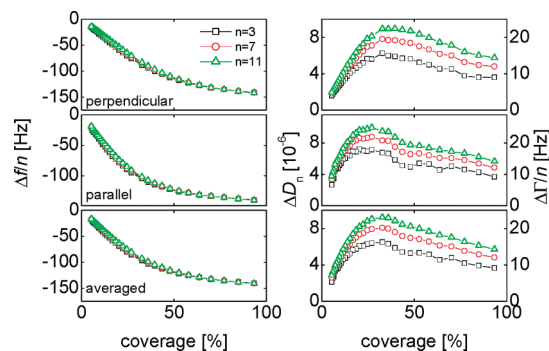


**Figure 5.** Dependence of  $\Delta f/n$  (left) and  $\Delta D_n$  (right) on coverage. These results were obtained with configuration I (soft spacer layer ( $|\eta_{\text{layer}}| = 2.15$  mPa s) and a hard sphere ( $|\eta_{\text{part}}| = 10^5$  mPa s)). The top and the center contain the results obtained with the flow perpendicular and parallel to the cylinder axes, respectively. The bottom panel shows the arithmetic averages. As expected,  $\Delta f$  saturates for large coverages, because of the effect of trapped solvent. There is a pronounced maximum of the dissipation at moderate coverage.

applied at the left and right edges of the cell. Coverage is defined as the ratio between the diameter of the cylinder and the width of the cell. The width of the cell was varied between 30 nm (93% coverage) and 470 nm (6% coverage). Note that the array of adsorbed cylinders is periodic in the simulation, whereas in the experiments, the particles are arranged randomly on the surface (see Figure 3C).<sup>4</sup> The resulting speed of flow along the horizontal is shown in Figure 4B.

The flow parallel to the cylinder axes (perpendicular to the plane of the paper in Figure 4) was calculated using the 2D steady-state diffusion module. This approach exploits an analogy between the theory of laminar flow and the theory of diffusion. For parallel flow, there is only one component of speed, and the pressure vanishes identically. The flow profile is described by the diffusion equation, where the momentum density ( $\rho v$ , where  $\rho$  is the density and  $v$  is the speed) takes the role of concentration, the kinematic viscosity ( $\eta/\rho$ ) takes the role of diffusivity, stress takes the role of normal flow rate at an interface, and the inertial force ( $i\omega\rho v$ ) takes the role of a reaction rate.

The 2D nature of the calculation entails another problem that is related to the definition of surface coverage. For a layer of particles on the surface, the close-packed arrangement corresponds to a projected coverage of 91%. At this maximum coverage, there are still interstitial voids, where the resonator surface is exposed to the bulk. At a coverage of, for instance, 50%, the average nearest distance between two spheres is  $\sim 0.35d$ , where  $d$  is the sphere or cylinder diameter. For a layer, on the other hand, the maximum projected coverage is 100%, and at a coverage of 50%, the average distance between neighboring cylinders is equal to  $d$ . For these reasons, the location of the peak on the coverage scale (see Figures 5 and 6) may not be naively compared to the corresponding coverage at maximum dissipation in the experiment (see Figure 3A).

In our previous work, we remarked that there is a stress singularity at the three-phase line between the particle, the surface, and the liquid.<sup>25</sup> Such singularities have been extensively studied

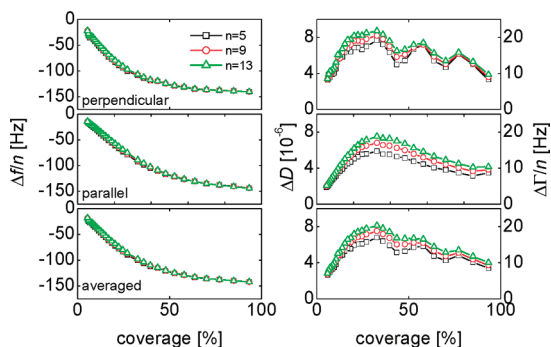


**Figure 6.** Dependence of  $\Delta f/n$  (left) and  $\Delta D_n$  (right) on coverage. These results were obtained with configuration II (a rigid planar layer ( $|\eta_{\text{layer}}| = 10^5$  mPa s) and a compliant particle ( $|\eta_{\text{part}}| = 100$  mPa s)). The top and the center contain the results obtained with the flow perpendicular and parallel to the cylinder axes, respectively. The bottom panel shows the arithmetic averages.

in the context of contact mechanics and fracture.<sup>43</sup> Their presence has several consequences:

(i) First, it necessitates the use of a fine mesh near the three-phase line. We forced the maximum mesh size to be 0.2 nm close to these boundaries. Otherwise, we used the default meshing. The limiting mesh size results from balancing numerical accuracy against computational resources. With an even finer mesh, COMSOL cannot handle the large cells needed to calculate the frequency shift at high dilution.

(ii) Second, it violates the assumptions upon which SLA is based. This is because SLA requires that the stress ( $\sigma = \dot{u}Z_1$ ) is small not only in the average sense, but also in the local sense. However, when a hard particle touches a hard surface, the local stress at the singularity may exceed this limit.<sup>25</sup> Therefore, a planar layer with a thickness of 2 nm was introduced between the resonator surface and the particle. The layer moves the stress singularity away from the resonator surface, where the stress is evaluated. Thus, the local stress (at the resonator surface) remains small in the sense of SLA, even if there is a large stress at the three-phase line. The spacer layer may even have the exact same mechanical properties as AT-cut quartz. Such a layer would have no physical significance, but it would move the singularity away from the plane of evaluation. Of course, the planar layer must be included in the calculation of the resonance frequency of the bare crystal. Otherwise,  $\Delta f$  would be nonzero in the absence of a particle due to the planar layer.

(iii) Finally, because of the high local stress at the three-phase boundary, even fairly stiff objects will deform in the regions that are close to the point of contact.<sup>25</sup> Both a somewhat compliant substrate and a somewhat compliant particle may, in conjunction with the stress concentration, act like a soft and deformable link. Alternatively, a soft linker molecule or a soft layer between the support and the particle may constitute such a link.

With regard to the viscoelastic parameters, two separate configurations were analyzed. In the first case (termed configuration I in the following), the particle was modeled as rigid. The planar layer was soft and, hence, acted as a deformable link. The particle was assigned moduli of  $G' = 1.6$  GPa and  $G'' = 0$ ,

independent of the overtone order. The linker layer was assigned a complex viscosity with a loss tangent of  $\delta = \arctan(\eta'/\eta'') = 30^\circ$ . The modulus of the viscosity  $|\eta|$  was varied between 1 mPa s and 1000 mPa s, which corresponds to moduli  $|G| = \omega|\eta|$  in the megapascal range (depending on the overtone order). In the second case (termed configuration II in the following), the planar layer was rigid ( $G' = 1.6$  GPa,  $G'' = 0$ , independent of overtone order) and, instead, the particle was assigned some softness. Again, the loss tangent was  $\delta = 30^\circ$  and  $|\eta|$  was varied between 1 mPa s and 1000 mPa s. In the second configuration, the near-surface portions of the particle act as the link.

As shown in ref 25, the FEM calculations readily reproduce both the Sauerbrey equation<sup>44</sup> and the Gordon–Kanazawa result,<sup>45,46</sup> with an error of  $<0.1\%$ . The film resonance in liquids<sup>47</sup> is reproduced within 1%. The shifts of frequency and bandwidth induced by sinusoidal corrugation gratings on the resonator surface, according to ref 48, are reproduced within 0.5 Hz, which amounts to a relative error of  $<5\%$  for corrugation amplitudes larger than 2 nm. We provide a further piece of validation in Appendix A, where we calculate  $\Delta f$  and  $\Delta \Gamma$  induced by a cylinder in close proximity to the resonator surface (but without a direct link). If such a cylinder is assigned a high density, it rests in place in the laboratory frame because of inertia.  $\Delta \Gamma$  can then be estimated analytically, using lubrication theory.<sup>49</sup> The agreement between the lubrication estimate and the FEM calculation is better than 2%.

We note that 3D FEM calculations should be possible with a more-powerful computer or other software packages that are geared more specifically toward computational fluid dynamics (CFD) than COMSOL. Interestingly, analytical calculations of the 3D flow around a single sphere located close to a rigid surface have been done in the 1960s by O'Neill<sup>50</sup> and by Brenner and co-workers.<sup>51</sup> This treatment applies to the limit of a dilute adsorbate. Possibly, it can be extended to account for a link. Such calculations would provide explicit equations, relating, for instance, the Df ratio to the softness of the link. The dilute state is a particularly interesting limit: hydrodynamic interactions with neighboring particles are absent; the corresponding Df ratio thus reflects the adsorbate's properties more directly, and its determination can provide interesting new insight into the adsorbate's mechanical behavior.

The model chosen for the FEM calculations certainly is not truly realistic in many ways. It ignores the 3D nature of the real experiment, surface roughness, nonspherical shapes, and all internal structure of the adsorbate. Even the use of continuum modeling is questionable if quantitative predictions are sought. Atomistic modeling is needed, should, for instance, the particle be attached to the substrate by some type of loose chain. Still, the chosen model captures some of the same essential features as those found in experiment. With regard to explaining these qualitative features, such a simple model is appropriate.

(44) Sauerbrey, G. Z. *Phys.* **1959**, *155*, 206.

(45) Borovikov, A. P. *Instrum. Exp. Techn.* **1976**, *19*, 223.

(46) Kanazawa, K. K.; Gordon, J. G., II. *Anal. Chim. Acta* **1985**, *99*, 175.

(47) Domack, A.; Prucker, O.; Rühle, J.; Johannsmann, D. *Phys. Rev. E* **1997**, *56*, 680.

(48) Urbakh, M.; Daikhin, L. *Phys. Rev. B* **1994**, *49*, 4866.

(49) Oron, A.; Davis, S. H.; Bankoff, S. G. *Rev. Mod. Phys.* **1997**, *69*, 931.

(50) O'Neill, M. E. *Chem. Eng. Sci.* **1968**, *23*, 1293.

(51) Goldman, A. J.; Cox, R. G.; Brenner, H. *Chem. Eng. Sci.* **1967**, *22*, 637.

(43) Anderson, T. L. *Fracture Mechanics: Fundamentals and Applications*; CRC Press: Boca Raton, FL, 2005.

## RESULTS AND DISCUSSION

**Shifts in Frequency and Dissipation.** The model outputs flow velocity fields in the specified geometry (e.g., Figure 4B), which are then used to calculate stresses and, ultimately, frequency and bandwidth shifts, according to eq 3. These are shown in Figures 5 and 6 for configurations I (rigid particle/compliant layer) and II (rigid layer/compliant particle), respectively. More specifically, we used a value of  $|\eta| = 2.15$  mPa s to describe layer compliance in the first configuration (Figure 5) and  $|\eta| = 100$  mPa s to describe particle compliance in the second configuration. The top and center panel of each figure show the data derived for a direction of flow perpendicular (top) and parallel (center) to the cylinder axes, respectively. The bottom panel shows the arithmetic average of the two.

These two figures are the central outcome of the FEM calculations. Essential features of the experimental data shown in Figure 3 are recovered in the FEM calculations: there is a peak in dissipation at an intermediate coverage, while such a peak is absent in frequency; the dissipation increases as the overtone order increases, while there is only little dependence of  $\Delta f/n$  on the overtone order.<sup>52</sup> Also, the magnitudes of  $\Delta f$  and  $\Delta D$  agree within 15% and a factor of  $<2$ , respectively. We note that the dissipation for a layer of soft particles is considerably higher than that of a homogeneous film with identical thickness and viscoelastic properties: the latter would be  $\sim 0.6 \times 10^{-6}$ .<sup>53</sup> This is a factor of 10 below the experimental value and the FEM result. We note also that the periodic features on the right-hand side of Figure 6, at coverages of 40% and 70%, are artifacts that are caused by the periodic arrangement of cylinders (which is unrealistic).

Two features in Figures 5 and 6 merit particular attention. First, both configurations (soft layer/rigid particle and rigid layer/soft particle) reproduce the experimental data. Therefore, from experimental data alone, one cannot deduce whether the softness should be attributed to the adsorbate, the substrate, or a separate linker between them. The weakest element dissipates. Therefore, our data suggest that the transient peak in dissipation is not limited to some particular configuration. Instead, it occurs for a wide variety of configurations, where the common characteristic is some softness of the contact region. Second, perpendicular flow (top panels) and parallel flow (middle panel) yield rather similar values of  $\Delta f$  and  $\Delta D$ , both for configuration I (Figure 5) and configuration II (Figure 6). We will see further below that the origin of dissipation is related to the particle motion, which is quite different for the two flow directions. Thus, this finding is not at all trivial.

**Locs of Energy Dissipation.** FEM calculations provide a wealth of detailed information about what is happening at the interface. This information is not accessible experimentally. Because our calculations reproduce the experimental observations, they can shed light on the mechanisms underlying the experimental responses. We begin with the energy dissipation. The maps shown in Figure 7 provide visual insight into the spatial distribution of dissipated energy, which is given by



**Figure 7.** Map of the spatial distribution of dissipated energy for configurations I (left) and II (right). White areas have high rates of energy dissipation per unit volume.

$\eta[(\partial v_y/\partial x)^2 + (\partial v_x/\partial y)^2]$ . For configuration I (left), a substantial amount of dissipation inside the soft planar layer can be observed. As expected, the perfectly elastic particle does not exhibit any dissipation. In contrast, for configuration II (right), no dissipation inside the perfectly elastic planar layer is found; however, some dissipation inside the viscoelastic particle is noted. In both configurations, the map of dissipation is intriguingly complex. The highest amounts of energy are dissipated in the liquid surrounding the particles and in the softest regions: the layer, in the case of configuration I, and the particle close to the contact region, in the case of configuration II.

From the examination of these energy dissipation maps, it becomes clear that, without additional knowledge about the compliance of the adsorbed particle relative to that of its contact with the surface, it is not possible to tell where the energy will be dissipated. Thus, both configurations reproduce experimental observations equally well.

**Modes of Particle Motion.** In our previous work,<sup>25,26</sup> as well as that previously discussed, we remarked that a layer of adsorbed particles dissipates more energy than a homogeneous layer with equivalent viscoelastic properties. If the particle/surface contact is modeled as extremely stiff ( $G \approx 1$  GPa (from ref 25)), the dissipation in the liquid flowing around these (stationary) particles is quite modest. This is essentially the case described by Urbakh and Daikhin in their work:<sup>46</sup> liquid flowing around/through a stiff rough/porous network. More-realistic values that describe the viscoelastic properties of the particle/surface contact used here lead to higher dissipation values. The cause of this increased dissipation is the motion (rocking and sliding) of the adsorbed particles. From the FEM calculations, one can straightforwardly determine the type and amplitude of this motion. In Figure 8, we examine these properties as a function of the linker compliance (configuration I) at 20% surface coverage for perpendicular flow. To characterize rocking motion, the rotation of the particle was normalized to the rotation of the background fluid. As a measure of sliding motion, the particle's slippage was normalized to the speed of the substrate. In the absence of interaction with the substrate, both quantities would be unity. For a rigidly coupled particle, both quantities would be zero. Both rocking and sliding are substantial. They both decrease as the stiffness of the link increases.

Because of its very flow geometry, rotational movement will be absent for parallel flow. In this flow direction, dissipation thus originates from slippage of the cylinders, relative to the substrate surface (data not shown).

The panel on the lower right in Figure 8 shows the energy dissipated in the linker layer. Naturally, it decreases as the stiffness increases. However, as remarked previously, most of the energy

(52) Such a dependence was found in the experiments reported in ref 25. However, these experiments were conducted on vesicles, which are much softer than the particles investigated here. In this case, the deformability of bulk of the vesicles did play a role in addition to the properties of the contact zone.

(53) This calculation made use of eq 7 in ref 2.

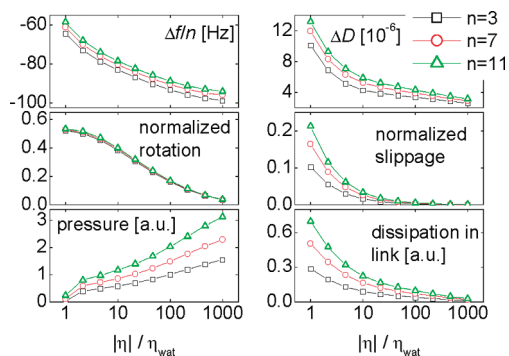


**Figure 8.** Dependence of various outputs of the FEM solution for configuration I on the stiffness of the spacer layer. The coverage was 20%. The normalized rotation is the speed of rotation of the sphere divided by the rotation of the background fluid. The normalized slip is the difference in speed between the substrate and the bottom of the sphere, divided by the speed of the substrate. The pressure was averaged over the linker layer. The dissipation was integrated over the linker layer. The amplitudes of rotation and slippage, as well as the dissipation in the link, all decrease with stiffness, paralleling the decrease in  $\Delta D$ .

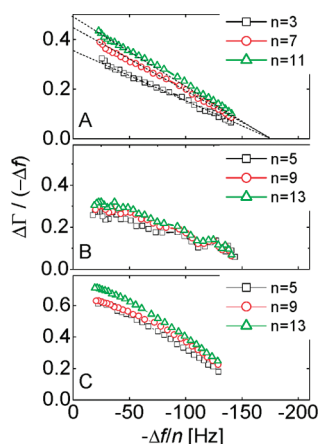


**Figure 9.** Df ratios, extracted from the bottom panels of (A) Figure 5 and (B) Figure 6, versus  $-\Delta f/n$ . Panel C shows the Df ratio for a scenario identical to that described in Figure 6, but with a 10-fold softer sphere ( $|\eta_{\text{part}}| = 10 \text{ mPa s}$ ).

is dissipated in the liquid surrounding the particles. That is to say, more energy is dissipated in liquid flowing around particles that can move (soft particle/surface contact) than in liquid flowing around the stationary objects.

The lower left panel shows the averaged modulus of the pressure ( $|p|$ ), where the average was taken over the entire linker layer. We elaborate on hydrostatic pressure in Appendix B. For comparison, the corresponding dependence of  $\Delta f$  and  $\Delta D$  on the compliance of the spacer layer is also displayed. As expected, the dissipation decreases as the linker stiffness increases.

**Coverage Dependence of the Df Ratio.** With increasing coverage, hydrodynamic interactions between adjacent particles will reduce the amplitude of motion (both rotation and slippage). The overall dissipation will thus decrease, resulting in the transient peaks in Figures 5 and 6 and a decrease in the Df ratio. Figure 9 displays the simulated data in another way, by emphasizing the intrinsic mechanical properties of the layer. The Df ratio, which is defined as the ratio of  $\Delta\Gamma/n$  (which is defined as  $2.5 \times 10^6 \text{ Hz} \times \Delta D$  for a 5 MHz crystal) and  $-\Delta f/n$ , was plotted versus  $-\Delta f/n$ . Panels A and B in Figure 9

correspond to Figures 5 and 6, respectively. Panel C in Figure 9 shows the result for a hard spacer layer and a soft particle, where the particle's viscosity was 10 mPa s (rather than 100 mPa s, as in panel B in Figure 9). Consistent with the experiments,<sup>26</sup> the Df ratio decreases as the coverage increases, and the decrease is almost linear; extrapolation of the lines (dashed lines in Panel A in Figure 9) for different overtones lead to a common intercept close to the y-axis. On a quantitative level, the extrapolated frequency shift at vanishing Df ratio is, for instance,  $-175 \text{ Hz}$  in Figure 9A, which corresponds to a Sauerbrey thickness of 31 nm. Again, as observed in the experiment, this value is very similar to the particle diameter (28 nm). The data shown in Figure 9 allow for extrapolation to  $\Delta f/n = 0$  as well, which yields the limiting Df ratio at high dilution. The limiting Df ratio increases as the overtone order and the softness of the link each increase. Its magnitude matches the experimental data in Figure 3. As Figures 9B and 9C show, the decrease in the Df ratio with  $-\Delta f/n$  is not always strictly linear. While one may be tempted to assign a meaning to the curvature (which also occurs in some experiments), this question is outside the scope of this work.

**Potential Further Applications.** This study shows that the response in bandwidth or dissipation of the QCM upon adsorption of discrete particles reflects the properties of the contact or linker region between the particle and the substrate, rather than the properties of the adsorbed particle itself. This finding can most likely be generalized in the sense that, for molecules that are composed of a series of rather rigid globules with soft interlinks, the dissipation originates essentially from the compliance of the links. For example, rather high dissipation values are commonly observed for IgG antibodies.<sup>54</sup> Here, two globules (the Fab domains) are connected via rather flexible hinges to a third globule (the Fc domain), resulting in a Y-shaped assembly. Upon adsorption, typically at least one of the globules is not in direct contact with the underlying support and, therefore, is free to move around the hinge.

Interestingly, our findings could be exploited to devise assays for the specific investigation of contact or linker regions. The properties of the linker region(s) might change after adsorption in response to environmental stimuli or in response to the addition of other small molecules that interact specifically with the link. In this type of experiments, the particle mostly serves as a tag. The link governs the dynamics of the particle and thereby becomes accessible to the experiment.

## CONCLUSIONS

Our results illustrate that the way by which nanosized objects are connected to the surface strongly influences the dissipation or bandwidth that is measured by quartz crystal microbalance (QCM). While much of the energy is dissipated in the liquid, the liquid flowing around the adsorbed particles causes them to move. The rest of the energy is dissipated in the contact zone between the particles and the surface, which deforms because of this motion. Increased dissipation occurs if the contact zone is narrow and contains a compliant element.

(54) Höök, F.; Vörös, J.; Rodahl, M.; Kurrat, R.; Böni, P.; Ramsden, J. J.; Textor, M.; Spencer, N. D.; Tengvall, P.; Gold, J.; Kasemo, B. *Colloids Surf. B* 2002, 24, 155.

In particular, much, if not all, of the dissipation that is typically observed for globular proteins or other nanosized objects of sufficient rigidity arises from the presence of a narrow, soft contact zone. Pronounced dissipation results, irrespective of the exact location of the compliant element—in the particle, on the surface, or between both (in the form of a linker).

A transient peak in dissipation that occurs during the adsorption of spherical objects to the surface of an acoustic resonator can be explained by a soft contact zone in conjunction with hydrodynamic interactions. With increasing coverage, hydrodynamic interactions between adjacent particles increasingly reduce rotation and slippage, thereby decreasing the overall energy dissipation.

## ACKNOWLEDGMENT

His-tagged GFP was kindly provided by Steffen Frey (Max Planck Institute for Biophysical Chemistry, Göttingen, Germany). IR and RPR gratefully acknowledge funding from the Department of Industry of the Basque Government. The work was also supported by the German Federal Ministry of Education and Research (BMBF, under Project No. 0315157).

## APPENDIX A: VALIDATION OF FEM CALCULATIONS WITH A LUBRICATION ESTIMATE

The force of friction between a cylinder and a plate can be calculated from lubrication theory (a) if the cylinder is at rest, while the surface moves with a known velocity (or vice versa), (b) if the cylinder is much smaller than the penetration depth of the shear wave, and (c) if the minimum distance between the cylinder and the plate ( $D$ ) is much less than the radius of the cylinder ( $R$ ). The second condition ensures that the motion of the cylinder may be approximated as a steady movement. The force of friction can then be converted to a shift in bandwidth (see eq A-7). The third condition entails a separation of length scales. The ensuing simplifications are exploited in the frame of the “lubrication theory”.<sup>47,55</sup>

The height of the gap between the crystal and the cylinders  $h(x,t)$  is given by

$$h(x,t) = D + \frac{(x - \dot{u}t)^2}{2R} \quad (\text{A-1})$$

Here,  $\dot{u}$  is the speed of motion. Lubrication theory supplies an ordinary differential equation for the pressure distribution  $p(x)$ , namely,

$$\frac{\partial}{\partial x} \left( h^3 \frac{\partial p}{\partial x} \right) = 6\eta \frac{\partial h}{\partial t} = -6\eta \dot{u} \left( \frac{x}{R} \right) \quad (\text{A-2})$$

which is solved by

$$p(x) = \frac{2\eta \dot{u} x}{h^2} \quad (\text{A-3})$$

This solution satisfies  $p = 0$  at  $x = \pm\infty$ . The flow field ( $v(x,z)$ ) is a superposition of shear flow and pressure-driven flow:

$$v(x,z) = \frac{\partial p}{\partial x} \frac{(z^2 - zh)}{2\eta} + \dot{u} \left( \frac{z}{h} \right) \quad (\text{A-4})$$

The first term is parabolic in  $z$ , as predicted by Poiseuille, whereas the second is linear, as in Couette flow. We have chosen a coordinate frame moving with the substrate. The stress at the resonator surface ( $\sigma(x)$ ) is given as

$$\sigma(x) = \eta \frac{\partial v}{\partial z} \Big|_{z=0} = -\frac{h}{2} \frac{\partial p}{\partial x} + \eta \left( \frac{\dot{u}}{h} \right) = \frac{2\eta \dot{u}}{h^2} \left( \frac{x^2}{R} \right) \quad (\text{A-5})$$

Inserting  $h$  from eq A-1 and integrating over  $x$  from  $-\infty$  to  $\infty$  yields the force of friction per unit width ( $F_{\text{fric}}$ ):

$$F_{\text{fric}} = 2\eta \pi \dot{u} \sqrt{\frac{2R}{D}} \quad (\text{A-6})$$

The shift in bandwidth ( $\Delta\Gamma$ ) is given as

$$\Delta\Gamma = \frac{1}{\pi Z_q} \left( \frac{F_{\text{fric}}}{L \dot{u}} \right) = \frac{2\eta}{L Z_q} \sqrt{\frac{2R}{D}} \quad (\text{A-7})$$

Here,  $L$  is the length of the simulation box ( $L \gg R$ ) and  $F/L$  is the area-averaged stress. The dashed line in Figure A-1B is  $\Delta\Gamma$ , according to eq A-7. The agreement with the FEM calculation is excellent. Note that the cylinder used for comparison with lubrication theory had an unrealistically high density ( $\rho = 10^6$  g/cm<sup>3</sup>) to fix its position in space. In experiment, one would have to fix the cylinder by mechanical means. Interestingly,  $\Delta f$  is positive for a cylinder clamped in space. Positive frequency shifts are the consequence of an elastic particle–plate interaction, when the particle is in air.<sup>56,57</sup> In liquid, the “elastic” interaction (that is, an in-phase restoring force) between the particle and the plate is caused by hydrostatic pressure.

Figure A-1 also shows results for cylinders with realistic densities (1 and 19 g/cm<sup>3</sup>, where the latter would correspond to a gold nanoparticle). For free cylinders with realistic densities,  $\Delta f$  is negative. As a consequence, one expects

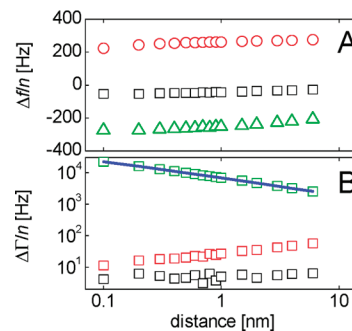


**Figure A-1.** Shifts of (A) frequency and (B) bandwidth for a cylinder located above a resonator surface with no link between the surface and the sphere. The cylinder diameter was 28 nm, the width of the cell was 140 nm, and the overtone order was  $n = 3$ . Symbols correspond to cylinder densities of ( $\square$ )  $\rho = 1$  g/cm<sup>3</sup> (a typical organic material), ( $\circ$ )  $\rho = 19$  g/cm<sup>3</sup> (gold), and ( $\triangle$ )  $\rho = 10^6$  g/cm<sup>3</sup> (an unrealistically high value, ensuring that inertia fixes the cylinder in space). When the cylinder is fixed in space,  $\Delta\Gamma$  can be estimated from lubrication theory (see eq A-7, represented by the dotted line in panel B). The agreement is better than 2%.

(55) Batchelor, G. K. *An Introduction to Fluid Mechanics*; Cambridge University Press: Cambridge, U.K., 1976.



**Figure B-1.** Map of the pressure distribution for configuration I (left) and configuration II (right). The white line indicates the range of integration of the pressure gradient (see Appendix B for details).

negative frequency shifts for a resonator exposed to a colloidal dispersion of non-adsorbing particles.<sup>58</sup> However, dispersions cannot be viewed as Newtonian liquids with a somewhat increased viscosity. That point has been made, for instance, by Horn et al.<sup>59</sup> The matter is more complicated because of diffusion, momentum relaxation, and momentum diffusion in the liquid. In low-frequency rheology, these processes occur on a time scale separate from the experiment. At high frequencies, the time scales are comparable, which changes the scenario on a fundamental level.

## APPENDIX B: COMMENTS ON HYDROSTATIC PRESSURE

The occurrence of hydrostatic pressure is characteristic of heterogeneous surfaces. For pure shear flow, the pressure is constant and identical to the pressure of the environment. Pressure and gradients thereof add a qualitatively new feature to the pattern of forces and displacements. The distribution of pressure for the geometry under consideration here is shown in Figures B-1A and B-1B for configurations I and II, respectively. The direction of flow is perpendicular to the cylinder axes. The pressure distributions for both configurations are quite similar. Pronounced pressure gradients can be identified at the contact line between the particle and the support.

The maximum pressure is 250 Pa. This value is characteristic for the small oscillation amplitudes chosen in our FEM model and must be adjusted to account for realistic oscillation amplitudes. The amplitude of oscillation ( $u_0$ ) is approximately<sup>16,60</sup>

$$u_0 = \frac{4}{n^2 \pi^2} (d_{26} Q U_{el}) = (1.25 \text{ pm/V}) \left( \frac{1}{D n^2} \right) U_{el} \quad (\text{B-1})$$

Here,  $d_{26}$  is the piezoelectric strain coefficient ( $d_{26} = 3.1 \times 10^{-12}$  pm/V),  $Q$  the quality factor,  $D$  the dissipation ( $D = 1/Q$ ), and  $U_{el}$  the driving voltage. In liquids, one typically chooses a large driving voltage because the system is heavily damped. Inserting, for instance, a value of  $U_{el} \approx 0.3$  V and a dissipation of  $D \approx 300 \times 10^{-6}$  leads to  $u_0 \approx 1.3$  nm. The FEM calculation (yielding a peak pressure of 250 Pa) was conducted assuming a value of  $u_0 \approx 0.1$  nm. Therefore, an amplitude of 1.3 nm induces a peak pressure of  $3 \times 10^3$  Pa  $\approx$  0.03 bar.

Pressure gradients have some importance beyond the immediate scope of this work; therefore, we slightly digress with regard to further implications of hydrostatic pressure. It has repeatedly been claimed that the quartz resonator's shear oscillation might have an influence on the adsorption of particles,<sup>61</sup> or even cause their desorption.<sup>62</sup> One may be tempted to suggest that the hydrostatic pressure, and gradients thereof, provide an important contribution to such effects. In this context, it is instructive to compare the contributions of pressure gradients and viscous drag to the overall force balance. The ratio of pressure gradient to viscous stress is independent of amplitude. As an example, we have integrated the normal component of the pressure gradient ( $\nabla p$ ) at the white line in Figure B-1, which gives a value of 2 mN/m.<sup>63</sup> The normal component of the viscous stress ( $\eta \nabla^2 v$ ), on the other hand, integrates to a value of 24 mN/m. This calculation suggests that the overall influence of hydrostatic pressure is only moderate. We conjecture that nonlinear effects, such as a Reynolds stress,<sup>64</sup> are more important.

Received for review June 25, 2009. Accepted August 27, 2009.

AC901381Z

(56) Dybwad, G. L. *J. Appl. Phys.* **1985**, *58*, 2789.  
 (57) Laschitsch, A.; Johannsmann, D. *J. Appl. Phys.* **1999**, *85*, 3759.  
 (58) Bell, J.; Köhler, T.; Woermann, T. *Ber. Bunsen. Phys. Chem.* **1997**, *101*, 879.  
 (59) Horn, F. M.; Richtering, W.; Bergenholtz, J.; Willenbacher, N.; Wagner, N. J. *J. Colloid Interface Sci.* **2000**, *225*, 166.  
 (60) Borovsky, B.; Mason, B. L.; Krim, J. *J. Appl. Phys.* **2000**, *88*, 4017.

(61) Edvardsson, M.; Rodahl, M.; Hook, F. *Analyst* **2006**, *131*, 822.  
 (62) Cooper, M. A.; Dultsev, F. N.; Minson, T.; Ostanin, V. P.; Abell, C.; Klenerman, D. *Nat. Biotechnol.* **2001**, *19*, 833.  
 (63) The pressure gradient has units of N/m, because the simulation is conducted in two dimensions. Otherwise, an integrated pressure gradient would be a force.  
 (64) Lighthill, J. *J. Sound Vib.* **1978**, *61*, 391.  
 (65) Richter, R. P.; Mukhopadhyay, A.; Brisson, A. *Biophys. J.* **2003**, *85*, 3035.